Chinese Chemical Letters 34 (2023) 107492

Contents lists available at ScienceDirect

Chinese Chemical Letters

journal homepage: www.elsevier.com/locate/cclet

Aggregation-induced emission meets magnetic bistability: Synergy between spin crossover and fluorescence in iron(II) complexes

Yao Li[a,1], Mohammad Khurram Javed[a,1], Shu-Qi Wu[b], Arshia Sulaiman[a], Ying-Ying Wu[a], Zhao-Yang Li[a,*], Osamu Sato[b], Xian-He Bu[a]

[a] School of Materials Science and Engineering, Nankai University, Tianjin 300350, China
[b] Institute for Materials Chemistry and Engineering, Kyushu University, Fukuoka 819-0395, Japan

ARTICLE INFO

Article history:
Received 26 March 2022
Revised 13 April 2022
Accepted 6 May 2022
Available online 10 May 2022

Keywords:
Magnetic bistability
Spin crossover
Luminescence
Aggregation-induced emission
Supramolecular structures

ABSTRACT

Luminescent spin crossover (SCO) materials have attracted significant interest owing to their potential applications in magneto-optical switches. However, the majority of previously reported Fe^{II}-based SCO complexes are adversely affected by fluorescence quenching in the solid-state. Here, we have constructed the first mononuclear Fe^{II} complex decorated with an aggregation-induced emission (AIE) luminophore (*i.e.*, tetraphenylethylene) that exhibits synergistic SCO and fluorescence behavior. Intriguingly, we obtained two types of crystals in different solvent systems, both displaying distinct magnetic bistability and fluorescence properties. The fluorescence intensity was observed to track the magnetic susceptibility, which confirmed that SCO and solid-state fluorescence operate synergistically. We introduce a novel approach for the construction of luminescent SCO compounds using an AIEgen as a luminophore, which leads to fluorescence emission in the solid-state, thus allowing us to study the synergy between SCO and fluorescence.

The spin crossover (SCO) phenomenon has received growing attention over the past few decades, primarily because of its potential applications in advanced electronic devices, including display devices, memory devices and switches [1–4]. SCO complexes can switch reversibly between low spin (LS) and high spin (HS) states in response to external conditions, with their electrical, optical, and mechanical properties changing dramatically as a result. In the past, SCO materials have been endowed with various physical properties, such as electrical conductivity, nanomagnetism, liquid crystals, and nonlinear optical properties, leading to the integration of multiple functionalities within a single material [5–9]. In particular, bifunctional luminescent SCO materials have received significant attention because they can track fluorescence signal modulation through spin-state switching processes. Conversely, spin-state switching activity can be detected using fluorescence. Despite extensive research over the past decade, luminescent SCO compounds that successfully demonstrate synergy are relatively rare, as transition metal ions (especially Fe^{II}) frequently lead to quenching of the luminescence. Two strategies have commonly been used to impart a material with luminescence and SCO synergy: the first involves directly coordinating a luminophore to an SCO transition metal ion, while the second consists of doping or covalently grafting a fluorophore into an SCO thin film and/or nanomaterial. The first strategy is arguably more efficient, as it leads to single crystals suitable for structural analysis. Garcia *et al.* were the first to report a bifunctional luminescent SCO complex characterized by crystallographic studies [10].

Currently, the majority of bifunctional luminescent SCO materials include fluorophores such as pyrene [11], naphthalene [12] and anthracene [13]. Our design strategy involves taking advantage of a luminophore that can strongly fluoresce in the solid-state. Therefore, we selected tetraphenylethylene (TPE), a well-known aggregation-induced emission (AIE) fluorophore (or AIEgen), because of its unique structural characteristics and strong fluorescence in the solid-state. TPE derivatives have been extensively investigated for applications in areas such as fluorescence sensors, light-emitting materials, and cell imaging [14,15]. Moreover, TPE fluorophores can be easily tethered to SCO ligands through Schiff base reactions, thus facilitating bifunctional properties in a single material. Using this approach, we coordinated TPE to 4-amino-3,5-bis(pyridin-2-yl)-1,2,4-triazole (abpt), an excellent SCO moiety, to incorporate both SCO and fluorescence into our compound. To the best of our knowledge, two-dimensional coordination polymers containing a TPE derivative (TPPE) are the only existing examples

* Corresponding author.
E-mail address: zhaoyang@nankai.edu.cn (Z.-Y. Li).
[1] These authors contributed equally to this work.

https://doi.org/10.1016/j.cclet.2022.05.006
1001-8417/

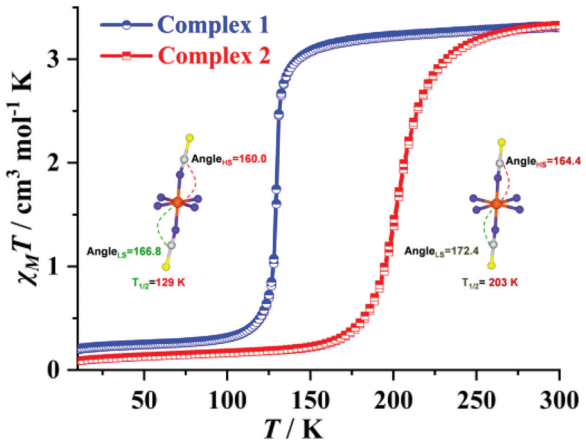

Fig. 1. Magnetic susceptibilities ($\chi_M T$) of [Fe(abpt-TPE)$_2$(NCS)$_2$]·4MeCN (**1**) and [Fe(abpt-TPE)$_2$(NCS)$_2$]·2MeCN·2CH$_2$Cl$_2$ (**2**) as a function of temperature (T). Inset: Structures showing the differences in the Fe−N$_{isothiocyanate}$−C angles (°) of **1** (left) and **2** (right) are also shown.

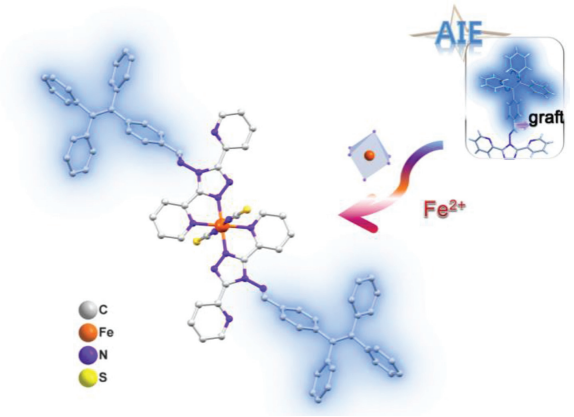

Fig. 2. Schematic diagram showing the structural design of [Fe(abpt-TPE)$_2$(NCS)$_2$] at the molecular level. Hydrogen atoms and solvent molecules have been omitted for clarity.

of AIEgen-based luminescent SCO compounds [16,17], whereas no examples of mononuclear bifunctional luminescent SCO complexes linked to AIEgens have been reported.

Thus, we herein report the synthesis of the novel ligand *N*-(3,5-di(pyridin-2-yl)-4*H*-1,2,4-triazol-4-yl)-1-(4-(1,2,2-triphenylvinyl)phenyl)methanimine (abpt-TPE) and its characterization by nuclear magnetic resonance (NMR) spectroscopy (Fig. S1 in Supporting information). Subsequently, the obtained ligand was coordinated to Fe^{II} in a bidentate manner along with two isothiocyanate anions to give [Fe(abpt-TPE)$_2$(NCS)$_2$]·4MeCN (**1**) and [Fe(abpt-TPE)$_2$(NCS)$_2$]·2MeCN·2CH$_2$Cl$_2$ (**2**). Both of these complexes exhibited SCO and fluorescence synergy in the aggregated state, although their spin transition temperature ($T_{1/2}$) differed by 74 K. Most reported luminescent SCO complexes only show synergy between the two properties around their $T_{1/2}$ value [16–20], whereas a few examples show synergy in the entire SCO temperature range [21–23]. Complexes **1** and **2** showed synergistic behavior between fluorescence and magnetic susceptibility over the entire temperature range of 80–300 K, which is rare and highly desirable. To the best of our knowledge, this is the first report that describes mononuclear AIE-SCO molecules.

To examine the magnetic behavior of the two complexes, magnetic susceptibility measurements were conducted on fresh samples of **1** and **2** in the temperature range of 10–300 K (swept at 5 K/min) under an applied magnetic field of 1000 Oe. Both complexes showed significant differences in their temperature-dependent magnetic data. Specifically, compound **1** exhibited abrupt and nearly complete one-step SCO behavior with a transition temperature ($T_{1/2}$) of 129 K. In addition, the $\chi_M T$ value of Fe$^{II}_{LS}$ increased from 0.21 cm^3 K/mol at 10 K to 3.24 cm^3 K/mol at 220 K, with a maximum of 3.30 cm^3 K/mol recorded at 300 K, which corresponds to Fe$^{II}_{HS}$ Meanwhile, complex **2** exhibited complete SCO behavior with a $T_{1/2}$ of 203 K; its $\chi_M T$ value increased from 0.08 cm^3 K/mol at 10 K to 3.30 cm^3 K/mol at 300 K, which is consistent with the presence of Fe$^{II}_{HS}$ Thus, as shown in Fig. 1, both **1** and **2** show one-step and abrupt SCO behavior, with a difference of ~74 K in their $T_{1/2}$ values; this behavior was reproduced in consecutive cycles.

Differential scanning calorimetry (DSC) was conducted on fresh samples of **1** and **2** to further characterize the SCO behavior. For complex **1**, upon cooling, a peak for the exothermic transition from the HS to the LS state was observed at 127 K with $\Delta H = 5.35$ kJ/mol and $\Delta S = 42.09$ J mol^{-1} K^{-1}. Upon heating, a peak for the endothermic transition from the LS to the HS state was observed at 128 K with $\Delta H = 3.80$ kJ/mol and $\Delta S = 30.00$ J mol^{-1} K^{-1}. For complex **2**, upon cooling, a peak for the exothermic transition from the HS to the LS state was observed at 199 K with $\Delta H = 10.82$ kJ/mol and $\Delta S = 54.38$ J mol^{-1} K^{-1}. Upon heating, a peak for the endothermic transition from the LS to the HS state was observed at 202 K with $\Delta H = 10.83$ kJ/mol and $\Delta S = 53.62$ J mol^{-1} K^{-1}.

Mössbauer spectroscopy (measured at 80 and 300 K for **1** and at 100 and 300 K for **2**) was used to further verify the Fe^{II} spin states of the two complexes (Fig. S3 in Supporting information). Quadrupole splitting (ΔE_Q) in the 0.497–0.513 mm/s range and isomer shifts (δ) in the 0.510–0.529 mm/s range were observed. These values are typical of Fe$^{II}_{LS}$ species, whereas values of 2.933–3.045 and 1.015–1.135 mm/s are usually observed for Fe$^{II}_{HS}$ species. Complex **1** is composed of ~79% Fe$^{II}_{LS}$ at 80 K, with the HS state accounting for ~21%, which means that some Fe$^{II}_{HS}$ is present in the low-temperature region. In addition, this LS to HS area ratio deviates slightly from that obtained from the magnetic data (0.94:0.06), which can be attributed to a loss of some solvent molecules [24]. In contrast, complex **2** is composed of 100% Fe$^{II}_{LS}$ at 100 K, and both **1** and **2** are composed of 100% Fe$^{II}_{HS}$ at 300 K, consistent with the magnetic susceptibility data (Table S1 in Supporting information).

The molecular structures of the two complexes were analyzed using single-crystal X-ray diffraction data obtained at 100 and 300 K. Complex **1** crystallizes in the monoclinic $P2_1/n$ space group, whereas complex **2** adopts the triclinic *P*-1 space group (Table 1). The asymmetric units of **1** and **2** contain one Fe^{II} center, one abpt-TPE ligand, and an isothiocyanate (NCS) moiety, and each complete structure is generated by inverting the Fe^{II} center, including the lattice solvents, with $Z = 2$ and 1, respectively. The Fe^{II} ions in both complexes adopt N_6 octahedral coordination arrangements linked by four nitrogen atoms *via* abpt-TPE units and two nitrogen atoms from two *trans*-NCS anions (Fig. 2). The average Fe–N distances in complexes **1** and **2** were determined to be 1.9821 and 1.9756 Å at 100 K, respectively, which are consistent with those in related Fe$^{II}_{LS}$ complexes containing abpt ligands [25,26]. To study the HS structures of the two complexes, we obtained single crystal structures for complexes **1** and **2** at 300 K. As shown in Table 1, the space groups of the two complexes remain unchanged in the HS state (*i.e.*, monoclinic $P2_1/n$ for **1** and triclinic *P*-1 for **2**). However, the average Fe–N distances of complexes **1** and **2** were determined to be 2.1544 and 2.1552 Å at 300 K (Table S2 in Supporting information), respectively, which agree with the Fe$^{II}_{HS}$–N distances reported in reference [11]. Moreover, **1** and **2** differ in their Fe–

Table 1
Crystallographic data for complexes **1** and **2**.

Complex	**1**		**2**	
Temperature (K)	100.00(10)	299.99(13)	100.00(10)	299.98(10)
Empirical formula	$C_{88}H_{68}FeN_{18}S_2$		$C_{86}H_{66}Cl_4FeN_{16}S_2$	
Fw	1497.57		1585.31	
Crystal system	monoclinic		triclinic	
Space group	$P2_1/n$		*P*-1	
a (Å)	8.92110(10)	8.9930(5)	8.0033(2)	8.0722(3)
b (Å)	19.0537(3)	19.2912(8)	12.4413(2)	12.6749(4)
c (Å)	22.0837(3)	22.7234(14)	20.4414(3)	20.9519(17)
α (°)	90	90	93.3410(10)	92.164(5)
β (°)	90	90	95.962(2)	96.427(5)
γ (°)	90	90	105.809(2)	106.447(3)
V (Å^3)	3753.79(9)	3942.2(4)	1939.81(7)	2037.6(2)
Z	2	2	1	1
ρ_{calcd} (g/cm^3)	1.325	1.262	1.357	1.292
F(000)	1560.0	1560.0	820.0	820.0
μ (mm^{-1})	2.611	2.486	3.786	3.604
GOF on F^2	1.032	1.034	1.089	1.107
R_1, wR_2 ($I > 2\sigma$ (I))	0.0520, 0.1373	0.0719, 0.1894	0.0504, 0.1479	0.0702, 0.2249
R_1, wR_2 (all data)	0.0593, 0.1424	0.1351, 0.2281	0.0526, 0.1497	0.0809, 0.2394

$N_{isothiocyanate}$–C angles, the dihedral angles (θ) of the four benzene rings of the abpt-TPE ligand, and their crystal packing.

The axial isothiocyanate ligands are slightly distorted from the Fe^{II} centers in **1** and **2** (Table S2). In the case of **1**, the Fe–$N_{isothiocyanate}$–C angles for the HS and LS structures of **1** were 160.01° and 166.77°, respectively, whereas those for the HS and LS structures of **2** were 164.36° and 172.40°, respectively. These results indicate that the Fe–$N_{isothiocyanate}$–C angles of **1** and **2** were larger in their LS states than in their HS states, and larger values were obtained for **2** than for **1** in the same spin state, which may have influenced the spin state.

The dihedral angles between the relevant planes in the ligands reflect the apparent different degrees of twisting of the TPE moiety in each compound. For elucidation, representative plane numbers are shown in Fig. S4 (Supporting information). The LS and HS dihedral angles for **1** differed by 0.906°–2.851°, whereas this difference was 0.974°–3.019° for **2**. However, the θ values for **1** and **2** are significantly different at 100 and 300 K (Table S3 in Supporting information), with differences of 19.986°, 7.351°, 35.31° and 12.69° at 100 K for $\theta_{Cg5\text{-}Cg6}$, $\theta_{Cg6\text{-}Cg7}$, $\theta_{Cg6\text{-}Cg8}$ and $\theta_{Cg6\text{-}Cg9}$, respectively, whereas these values were 16.061°, 7.413°, 29.819° and 13.154° at 300 K. The degrees of distortion of the TPE phenyl rotors may therefore play significant roles in affecting the SCO phenomena of **1** and **2** by slightly affecting the ligand field.

In addition to the observed differences in molecular geometry, the two complexes also show significantly different crystal packing. The lattice solvents of **1** and **2** are located in the resulting spaces (Figs. S5 and S6 in Supporting information). Both complexes form $\pi\cdots\pi$ stacking interactions between adjacent chains at 100 K that involve the pyridine rings of the abpt ligands and result in the formation of supramolecular 1D chains along the crystallographic *a* axis. In addition, the A and B chains of the complexes coordinate through hydrogen bonding. Complex **1** displays differently oriented linear A (green) and B (red) chains in the *bc* plane, which creates an alternating pattern involving the two chain types (Fig. 3a). The adjacent molecules interact with each other through C–H···N hydrogen bonding within each chain (A or B), as shown in Fig. S5, with an Fe–Fe distance of 19.054 Å between adjacent molecules, whereas the intermolecular Fe–Fe distance between adjacent A and B chains is 15.251 Å. Adjacent A chains are connected through $\pi\cdots\pi$ contacts between the pyridine moieties of adjacent complexes (Fig. 3b). Adjacent B chains are connected in a similar manner to the A chains but are oriented differently (Fig. 3c). In contrast, complex **2** forms 1D linear chains (Fig. 3d) that are arranged in a parallel BB (red) stacking pattern in the *bc* plane. The

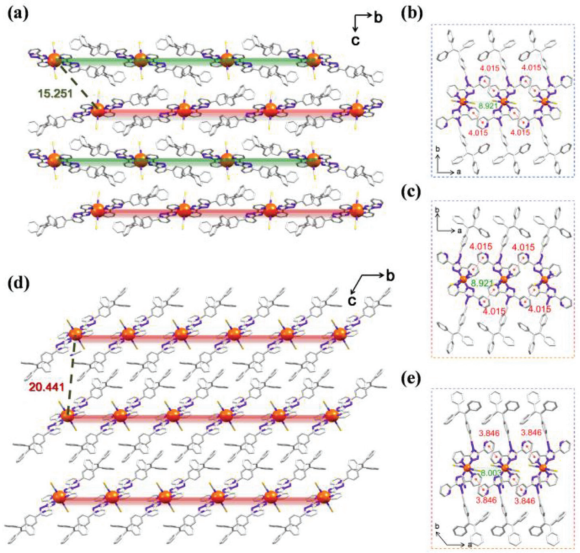

Fig. 3. Crystal packing in various directions for (a–c) **1** and (d, e) **2**. The numbers in the figure represent distances in angstroms.

complex interacts with neighboring molecules within each chain through CH···S and CH···N hydrogen bonds (Fig. S6), and the Fe–Fe distance between adjacent molecules is 12.441 Å, which is shorter than the analogous distance for **1**. On the other hand, the distance between the two iron centers in adjacent chains in the *bc* plane is 20.441 Å for complex **2**. As observed for **1**, the adjacent chains of **2** form $\pi\cdots\pi$ interactions in the *ab* plane (Fig. 3e) connected through the pyridine rings of the abpt-TPE ligands.

Despite their similar structures, the crystals of **1** and **2** are not isomorphous and can be interconverted using a variety of solvent mixtures. Needle-like crystals of complex **2** were obtained by immersing the crystals of **1** in 2:1:1 (v/v/v) methanol/dichloromethane/acetonitrile and allowing the mixture to stand for several days. On the other hand, **2** was converted into **1** by immersing the crystals of **2** in 5:1 (v/v) acetonitrile/ethanol with continuous heating for 2 h followed by slow evaporation. Interconversion between these two compounds was confirmed by single-crystal X-ray diffractometry and magnetic data. The TGA curve (Fig. S7 in Supporting information) showed that for complex **1**, the mass loss of compound **1** between 40 °C and 166 °C

can be attributed to the loss of four acetonitrile molecules (lattice solvents, observed 10.4%, calculated 11.0%). For complex **2**, the mass loss between 59 °C and 145 °C can be attributed to the loss of two molecules of dichloromethane and two molecules of acetonitrile (lattice solvents, observed 15.0%, calculated 15.9%). Room-temperature PXRD data for **1** and **2** were obtained and are consistent with the simulated data (Fig. S8 in Supporting information), thereby confirming the phase purities of these crystal samples. Moreover, the PXRD patterns of compounds **1** and **2** were found to be significantly different, which is indicative of significant structural differences.

Complexes **1** and **2** were also subjected to density functional theory (DFT) calculations to further explore the underlying reasons for the significant differences in their spin transition temperatures. Full geometric optimization was therefore employed with the molecular geometries from X-ray diffraction determination at 100 and 300 K for both polymorphs as the initial guesses. The solvent molecules were also eliminated from the original structure. Optimization provided almost identical final structures for the HS and LS states, regardless of the initial structures and their polymorphic phases (Tables S4 and S5 in Supporting information). The optimized LS and HS ground state structures of both complexes were found to be well aligned with the corresponding experimental data (Table S6 in Supporting information). As the Fe–$N_{isothiocyanate}$–C angle increased in the 155°–175° range, the energy of each HS state increased, whereas the energy of each LS state decreased (Fig. S9 in Supporting information). In addition, the Fe–$N_{isothiocyanate}$–C angles of HS- and LS-**2** were determined to be 164.36° and 172.40° from X-ray structures, which are larger than the corresponding values for **1** (160.01° and 166.77°, respectively). According to the potential energy scan of the Fe–$N_{isothiocyanate}$–C angle, complex **2** was of higher energy in the high-temperature phase and of lower energy in the low-temperature phase; consequently, the difference between the HS and LS energies was also greater. Consistent with its SCO behavior, complex **2** possessed a higher transition temperature based on the same entropy change, which is in agreement with the experimental data. These results suggest that the changes in the Fe–$N_{isothiocyanate}$–C angle are likely responsible for the different spin transition temperatures of **1** and **2**.

The luminescence behavior of abpt-TPE, **1**, and **2** was then investigated through solid-state fluorescence studies (Fig. S10 in Supporting information). The abpt-TPE ligand exhibited a strong emission at approximately $\lambda_{max} = 478$ nm when excited at 365 nm at room temperature, whereas **1** exhibited an emission at $\lambda_{max} = 465$ nm at the same excitation wavelength, which represents a blueshift of 13 nm compared to the emission of the ligand. In contrast, complex **2** showed only a slight blueshift along with a new band at approximately 615 nm. These results show that the fluorescence properties of abpt-TPE are well retained after chelation to the Fe^{II} ions.

Correlations between the SCO and the fluorescence behavior of the AIE-SCO compounds were then investigated by variable-temperature fluorescence-emission spectroscopy (Figs. 4a–c) tested in warming mode using fresh samples. The temperature-dependent fluorescence spectra of the abpt-TPE ligand showed single peaks at 478 nm in the 80–300 K temperature range. In addition, the intensity of the emission from the ligand was observed to gradually decrease with increasing temperature, which is ascribable to thermal fluorescence quenching, as is typically observed for fluorophores (Fig. 4d) [27]. As expected, both **1** and **2** exhibited significantly different fluorescence behavior. For **1**, two emission peaks were observed at $\lambda_{max} = 441$ and 465 nm at 100 K. The relative intensities of these two peaks gradually increased with increasing temperature in the temperature range of 100–220 K, above which the intensity of the $\lambda = 465$ nm emission overwhelmed that of the $\lambda = 441$ nm emission and reached a plateau (Fig. 4b). Notably, this observation is in good agreement with the magnetic susceptibility data of **1**, as the LS to HS transition occurs in the 100–220 K temperature range. At 220 K, the maximum intensity of fluorescence emission is approximately three times greater than at 100 K. Furthermore, the fluorescence intensity was found to decrease at temperatures > 220 K owing to thermal quenching, which is also in good agreement with the magnetic data, as it indicates that the Fe^{II}_{HS} state is consistently present above 300 K. In contrast, the intensity of the peak at $\lambda = 457$ nm observed at 100 K for **2** decreased as the temperature increased from 80 K to 190 K. However, upon further heating to 320 K, this emission increased in intensity and was redshifted by 17 nm ($\lambda = 474$ nm). At 320 K, the maximum intensity is approximately six times greater than that at 80 K. The initial decrease in intensity was therefore recovered at higher temperatures (Fig. 4c). These abnormal changes in intensity occur between 190 K and 320 K and almost correspond to the thermally induced spin transitions of **2**. Another weak emission was observed at 615 nm, which became more intense above 190 K and then decreased in intensity when the temperature exceeded 320 K. Thus, the fluorescence behavior of each complex is significantly affected by the spin transitions of the Fe^{II} ions, providing evidence that the SCO behavior can moderate the emission intensity.

Furthermore, the data summarized in Figs. 4e and f demonstrate how the fluorescence emission intensities of **1** and **2** track the magnetic susceptibility ($\chi_M T$), providing strong evidence of synergy. Correlations between the SCO and fluorescence behaviors primarily reveal the presence of two types of synergy [28]: (1) a synchronous correlation between fluorescence and SCO that is observed only at/around the SCO critical temperature, which is the case for most reported luminescent SCO compounds [16–20]; and (2) spin-state-dependent fluorescence emission that is observed over the entire temperature range, with LS-state quenching and enhanced HS-state fluorescence. The latter type, which represents an efficient synergistic correlation [21–23], was observed for the compounds in this study. Compared with the type (1), the fluorescence intensity of the compounds increased abnormally, and the SCO transition process occurred simultaneously in the latter type. SCO has a greater influence on the fluorescence intensity, which can be used to detect the SCO process with better fluorescence intensity changes. The reaction is more sensitive, and *vice versa*.

To elucidate the modulation mechanism that correlates SCO with fluorescence, time-dependent DFT calculations were used to determine the vertical transition energies and the corresponding transition probabilities (Tables S7 and S8 in Supporting information). The calculated absorption spectra for LS and HS are shown in Fig. 5. The strongest absorption band calculated for the LS state (centered at 436 nm) corresponds to the intraligand $\pi \rightarrow \pi^*$ transition of the abpt-TPE ligand, with a partial metal-to-ligand charge transfer (MLCT) contribution (Fig. S11 in Supporting information). The two calculated weak absorption bands in the higher wavelength region (centered at 529 and 705 nm) are derived from the $d(Fe) + \pi(SCN) \rightarrow \pi^*$ (abpt-TPE) transitions and are ascribable to MLCT (Figs. S12 and S13 in Supporting information). The bands calculated for the HS state (centered at 422 and 529 nm) agree with the experimentally observed bands found at 405 and 541 nm for complex **1** and at 420 and 550 nm for complex **2** (Fig. S14 in Supporting information). The former band mainly originates from an intraligand $\pi \rightarrow \pi^*$ transition (with a weak MLCT contribution), whereas the latter corresponds to $d(Fe) + \pi(SCN) \rightarrow \pi^*$ (abpt-TPE) transitions (Figs. S15 and S16 in Supporting information). Notably, the absorption bands in the 500–800 nm range were calculated to be significantly weaker than those of the LS state. In addition, the strongest absorption band observed for the HS state was blueshifted by approximately 15 nm compared to that observed for the LS state. Therefore, we conclude that the degree of absorption and fluorescence overlap is higher for the LS state than for the HS

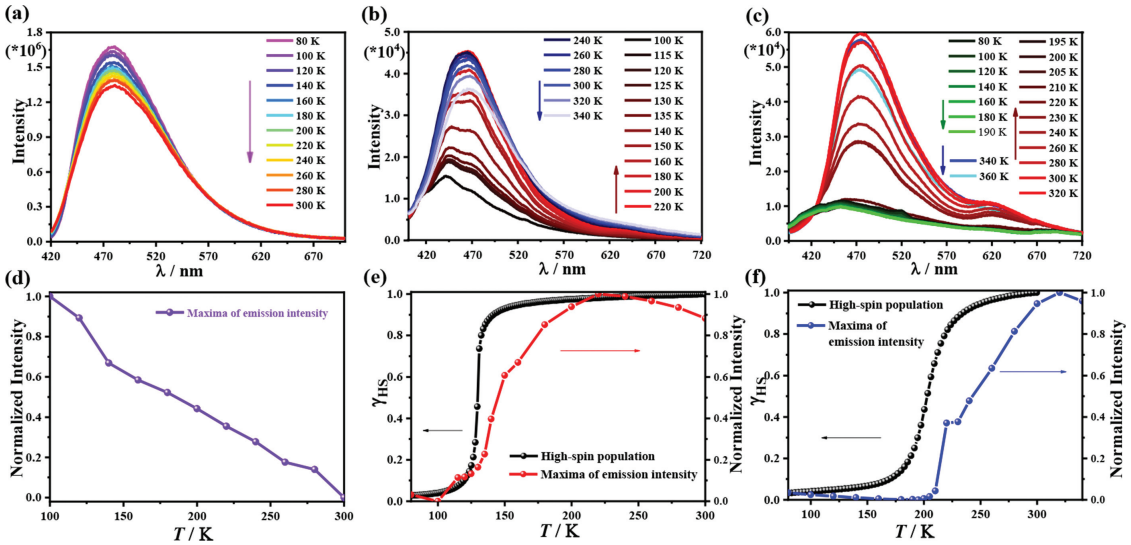

Fig. 4. Variable-temperature fluorescence-emission spectra of (a) abpt-TPE, (b) **1** and (c) **2**. (d) Normalized maximum fluorescence emission intensity as a function of temperature for the abpt-TPE. Normalized $\chi_M T$ values and fluorescence emission intensities of (e) **1** and (f) **2**.

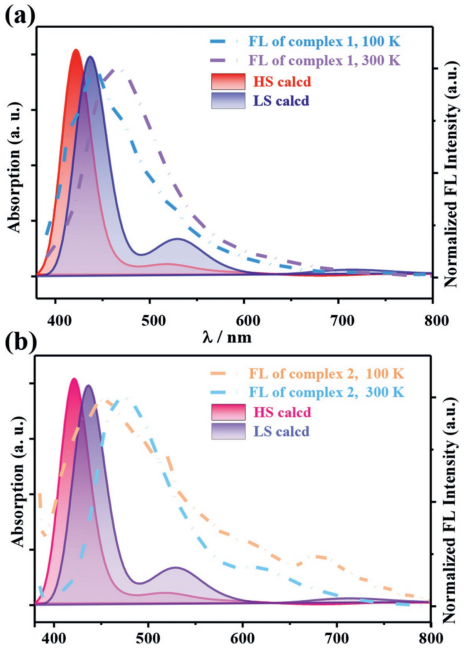

Fig. 5. TD-DFT-calculated absorption spectra for the HS and LS states of the optimized structure and the fluorescence emission spectra of (a) **1** and (b) **2** at 100 K and 300 K.

state. As a result, luminescence is enhanced during spin reversal from the LS to the HS state, with HS–LS-dependent fluorescence intensities being expected for the abpt-TPE ligand.

We reported two simple complexes in which the Fe^{II} ions are tethered to an aggregation-induced emission (AIE) luminophore (*i.e.*, tetraphenylethylene, TPE). Magnetic studies revealed that both complexes show spin crossover (SCO) behavior with a 74 K difference in their spin transition temperatures. This significant variation in the magnetic behaviors of the two complexes was ascribed to differences between the lattice solvents, crystal packing, and Fe–$N_{isothiocyanate}$–C bond angles. Importantly, the fluorescence spectra of the two compounds were notably affected by the spin transition, resulting in synergy between their SCO and fluorescence properties. Therefore, this study provides a valuable strategy for designing luminescent SCO molecules (AIE-SCO) by utilizing AIE-based fluorophores, which can emit strong fluorescence in the aggregated state and are conducive to the development of magneto-optical devices.

Declaration of competing interest

The authors declare that they have no known competing financial interests or personal relationships that could have appeared to influence the work reported in this paper.

Acknowledgments

We especially thank Nankai University for the startup funds in support of young talented researchers. Furthermore, this work was supported by the National Natural Science Foundation of China (NSFC, Nos. 21971124, 22035003).

Supplementary materials

Supplementary material associated with this article can be found, in the online version, at doi:10.1016/j.cclet.2022.05.006.

References

[1] O. Kahn, C.J. Martinez, Science 279 (1998) 44.
[2] O. Kahn, J. Kröber, C. Jay, Adv. Mater. 4 (1992) 718–728.
[3] H.J. Shepherd, C.M. Quintero, G. Molnár, L. Salmon, A. Bousseksou, Luminescent spin-crossover materials, in: M.A. Halcrow (Ed.), Spin-Crossover Materials: Properties and Application, John Wiley & Sons Ltd., 2013, pp. 347–373.
[4] O.I. Kucheriv, V.V. Oliynyk, V.V. Zagorodnii, et al., Sci. Rep. 6 (2016) 38334.
[5] C. Lefter, V. Davesne, L. Salmon, et al., Magnetochemistry 2 (2016) 18.
[6] K. Takahashi, H.B. Cui, Y. Okano, et al., J. Am. Chem. Soc. 130 (2008) 6688–6689.
[7] P.G. Lacroix, I. Malfant, J.A. Real, V. Rodriguez, Eur. J. Inorg. Chem. (2013) 615–627.
[8] Y. Bodenthin, G. Schwarz, Z. Tomkowicz, et al., J. Am. Chem. Soc. 131 (2009) 2934–2941.
[9] K.S. Kumar, M. Ruben, Coord. Chem. Rev. 346 (2017) 176–205.
[10] Y. Garcia, F. Robert, A.D. Naik, et al., J. Am. Chem. Soc. 133 (2011) 15850–15853.
[11] J.L. Wang, Q. Liu, Y.S. Meng, et al., Chem. Sci. 9 (2018) 2892–2897.
[12] J.L. Wang, Q. Liu, X.J. Lv, et al., Dalton Trans. 45 (2016) 18552–18558.
[13] P. Dierks, A. Päpcke, O.S. Bokareva, et al., Inorg. Chem. 59 (2020) 14746–14761.
[14] B. Jiang, C.W. Zhang, X.L. Shi, H.B. Yang, Chinese J. Polym. Sci. 37 (2019) 372–382.
[15] H.T. Feng, Y.X. Yuan, J.B. Xiong, et al., Chem. Soc. Rev. 47 (2018) 7452–7476.
[16] J.Y. Ge, Z. Chen, L. Zhang, et al., Angew. Chem. Int. Ed. 58 (2019) 8789–8793.
[17] Y.R. Qiu, L. Cui, J.Y. Ge, et al., Front. Chem. 9 (2021) 692939.

[18] J. Yuan, S.Q. Wu, M.J. Liu, O. Sato, H.Z. Kou, J. Am. Chem. Soc. 140 (2018) 9426–9433.
[19] Y. Jiao, J. Zhu, Y. Guo, W. He, Z. Guo, J. Mater. Chem. C 5 (2017) 5214–5222.
[20] J. Yuan, M.J. Liu, S.Q. Wu, et al., Inorg. Chem. Front. 6 (2019) 1170–1176.
[21] B. Benaicha, K.V. Do, A. Yangui, et al., Chem. Sci. 10 (2019) 6791–6798.
[22] C. Lochenie, K. Schötz, F. Panzer, et al., J. Am. Chem. Soc. 140 (2018) 700–709.
[23] T. Delgado, M. Meneses-Sánchez, L. Piñeiro-López, et al., Chem. Sci. 9 (2018) 8446–8452.
[24] J.J. Amoore, C.J. Kepert, J.D. Cashion, et al., Chem. Eur. J. 12 (2006) 8220–8227.
[25] C.H. Shih, C.F. Sheu, K. Kato, et al., Dalton Trans. 39 (2010) 9794–9800.
[26] C.F. Sheu, S.M. Chen, S.C. Wang, et al., Chem. Commun. (2009) 7512–7514.
[27] N. Sabbatini, M. Guardigli, I. Manet, F. Bolletta, R. Ziessel, Inorg. Chem. 33 (1994) 955–959.
[28] C.F. Wang, G.Y. Yang, Z.S. Yao, J. Tao, Chem. Eur. J. 24 (2018) 3218–3224.